Journal of Quantitative Spectroscopy & Radiative Transfer 251 (2020) 107039

Contents lists available at ScienceDirect

Journal of Quantitative Spectroscopy & Radiative Transfer

journal homepage: www.elsevier.com/locate/jqsrt

Bidirectional transmittance of transparent windows with external or backside condensation of nonabsorbing cap-shaped droplets

Yong Huang[a], Chenxi Feng[a], Jack Hoeniges[b], Keyong Zhu[a,*], Laurent Pilon[b,*]

[a] School of Aeronautic Science and Engineering, Beihang University, Beijing 100191, China
[b] Mechanical and Aerospace Engineering Department, University of California, Los Angeles, Los Angeles, USA

ARTICLE INFO

Article history:
Received 24 July 2019
Revised 19 April 2020
Accepted 19 April 2020
Available online 14 May 2020

Keywords:
Bidirectional transmittance distribution function
Fogging
Dropwise condensation
Visibility reduction
Image distortion

ABSTRACT

This study investigates systematically the effects of nonabsorbing droplets on the bidirectional transmittance of transparent windows. The Monte Carlo ray-tracing method was used to predict the bidirectional transmittance of transparent windows supporting monodisperse or polydisperse and randomly distributed droplets on their front side or backside. In both cases, photons that did not interact with the droplets were transmitted in the same direction as the incident direction. In addition, the bidirectional transmittance was found to be independent of the diameter and size distribution of the nonabsorbing droplets. It also featured cutoff transmission angles for certain ranges of incident and contact angles for either external or backside droplets. Analytical predictions of these cutoff angles were developed and were in excellent agreement with results from numerical simulations. Moreover, the bidirectional transmittance of the windows with either front or back side droplets increased with increasing projected surface area coverage at transmission angles other than the incident angle. The hemispherical distributions of the bidirectional transmittance showed that the photons scattered into other transmission azimuthal angle were concentrated in the angular region bounded by the cutoff angles for either external droplets or backside droplets.

© 2020 Elsevier Ltd. All rights reserved.

1. Introduction

Fogging is ubiquitous on surfaces of optical components and windows both in our daily life and in many technological applications [1–4]. Light scattering by water droplets hinders visibility, reduces performance, and may even create safety hazard [5]. Fogging typically develops when the temperature of optical windows is lower than the dew point temperature of the surrounding air. Then, water vapor in the air condenses on the surface to form dispersed water droplets. Such droplet condensation has significant negative effects on light transfer. For example, water droplets may condense on the inner surface of greenhouse covers [6] and solar desalination modules [7] as well as on the external surface of solar cells [8]. Then, the presence of droplets reduces the solar energy input and the system's energy efficiency due to reflection and/or absorption of the incident radiation by the droplets [9]. Fogging and rain also hinder the visibility through vehicle windshields [10] and architectural glass windows [11]. Furthermore, light scattering by condensed water droplets can cause severe image distortion on camera lenses used for navigation or surveillance [12] as well as on analytical and medical optical instruments [13].

The optical impact of droplets may be reduced significantly by modifying the wettability of optical window surfaces with either superhydrophilic or superhydrophobic coatings [5,14]. Superhydrophilic coatings, with droplet contact angle less than 5°, can be wetted completely to form a water film instead of distinct droplets [15,16]. The formation of a continuous water film reduces the refractive index mismatch between the air and the window, and thus increases slightly the transmittance of the window in the visible compared with situations when the surface is dry [17,18]. Alternatively, superhydrophobic coatings, resulting in water droplets with contact angle above 150° and extremely low contact angle hysteresis, causes the water droplets to quickly slide off the surface [19,20]. However, these different coatings have several drawbacks. First, they generally requires complicated and/or costly procedures to fabricate and/or their properties usually fade away over time [12,21]. Furthermore, antifogging coatings cannot fully prevent fogging under extreme conditions and may exhibit excessive and nonuniform water condensation [22–24].

Water droplets can be present either on the front side or on the backside of optical windows, depending on their location with respect to the direction of incident light. Front side or external

---

[*] Corresponding author.
E-mail addresses: zhukeyong@buaa.edu.cn (K. Zhu), pilon@seas.ucla.edu (L. Pilon).

https://doi.org/10.1016/j.jqsrt.2020.107039
0022-4073/© 2020 Elsevier Ltd. All rights reserved.

Nomenclature

d	droplet diameter, μm
d_m	mean diameter of droplets, μm
d_p	projected diameter of droplets, μm
f_A	projected surface area coverage of droplets
H	thickness of the window, mm
L	length of the window, mm
l_c	capillary length, mm
M	interval number of transmission angles
N	number of rays
n	refractive index
$\mathbf{n}$	unit vector of normal
$\mathbf{s}$	unit vector of ray direction
T_{bd}	bidirectional transmittance
$\overline{T}_{\text{bd}}$	one-dimensional bidirectional transmittance
$\overline{T}_{\text{bh}}$	one-dimensional directional-hemispherical transmittance
W	width of the window, mm

Greek symbols

θ	incident polar angle, °
θ_c	contact angle, °
θ_{cr}	critical angle for total internal reflection, °
σ	standard deviation of droplet diameter, μm
φ	azimuthal angle, °
ψ	angle of refraction, °
Ω	solid angle

Subscripts

a	refers to air
co	refers to cutoff angle
d	refers to droplet
i	refers to incidence
t	refers to transmission
w	refers to window

Superscripts

B	refers to backside droplets
E	refers to external droplets
$+$	refers to large cutoff angle
-	refers to small cutoff angle

droplets refer to the situation when droplets are present on the face of the optical windows exposed to the incident light. This is the case of rain on windshields as well as fogging of camera lenses and solar cells. On the other hand, droplets may also be present on the backside of windows in the case of fogging of the interior surface of residential buildings or vehicle windshields as well as during condensation on the inner cover of greenhouses and solar desalination systems. These two situations should be distinguished since the incident light interacts very differently with external and backside droplets [25].

Experimental measurements and numerical simulations of light transfer through windows with backside droplets were reviewed in details in our previous study and need not be repeated [26]. In brief, the normal-hemispherical transmittance of windows supporting droplets on their backside featured four distinct optical regimes defined with respect to the droplet contact angle and the critical angle for total internal reflection at the droplet/air interface. The normal-hemispherical transmittance increased slightly for contact angle smaller than the critical angle (Regime I) but decreased monotonously with increasing surface area coverage for contact angle larger than the critical angle (Regimes II, III, and IV) [26]. Briscoe and Galvin [27] presented an analysis to predict the normal-hemispherical transmittance of glass windows with backside condensation of water droplets and found that the decrease in the normal-hemispherical transmittance was due to total internal reflection at the droplet/air interface.

Few investigations have paid attention to the effect of external droplets on light transfer through optical windows [28]. In short, the directional-hemispherical transmittance of optical windows with external condensation of *nonabsorbing* droplets was nearly independent of droplet contact angle for incident angle smaller than 30°. However, it decreased monotonously with increasing incident angle and/or droplet contact angle for contact angle smaller than 70° to reach a minimum at a contact angle beyond which it increased with increasing contact angle before reaching a plateau at large contact angles ($>$ 150°). This was due to total internal reflection at the window back surface/air and droplet/air interfaces [25]. Moreover, for *absorbing* droplets either on the front or backside of the window, the normal-hemispherical transmittance decreased significantly with increasing droplet contact angle, mean diameter, polydispersity, and surface area coverage due to strong volumetric absorption within the droplets [25,29].

The directional-hemispherical transmittance for transparent and absorbing external or backside droplets previously reported [25,26,29] provided only the fraction of incident energy transmitted in all directions through the window supporting the droplets. However, these previous studies did not provide the angular distribution of the transmission radiation described by the so-called bidirectional transmittance. The latter is an essential optical characteristics in various applications including light transfer in greenhouses [30,31], solar distillation systems or solar stills [32–34], photobioreactors (PBRs) [35,36], and optical imaging systems [37]. Light scattering by droplets in these different systems leads to the redistribution of sunlight in all directions which can significantly affect the systems' performances. For example in greenhouses, direct collimated solar radiation can scorch leaves while scattered light penetrates deeper into the canopy, thereby increasing absorption of sunlight by plants to carry out photosynthesis [38].

In addition, Fig. 1(a) illustrates the principle of solar stills consisting of heating salty or brackish water with solar radiation resulting in water evaporation and subsequent condensation of water droplets onto the colder window. The latter traps the incoming solar radiation inside the still and serves as a condensing surface [32]. The condensate is collected at the bottom of the inclined window as drinking water. Here, the transmittance of the window decreases due to the presence of condensed droplets which significantly reduces the yield of the system [32]. Indeed, light scattering by droplets increases reflection of the incident solar radiation [32] thus decreasing the overall heat input and the water evaporation rate [33,34]. The surface coverage of the droplet and their contact angle on the condensation surface and the angle of incidence of the sunlight with respect to the normal vector to the window were found to play a very important role [32,33].

Similar transport processes take place in outdoor photobioreactors such as race ponds or photobioreactors covered by a plastic window to prevent contamination, as illustrated in Fig. 1(b). Here, changes in the direction of the transmitted light due to the presence of droplets will affect how light is absorbed in the PBR volume. For example, normal incidence allows deep penetration of the light into the PBR volume, whereas oblique incidence has been shown to reduce exposure of the culture to light [35,36]. Thus, knowledge of the bidirectional transmittance of the droplets covered the window is essential for quantifying the impact of droplets on PBR performance.

Moreover, light scattering by droplets condensed on optical windows, for example, eyeglasses, camera lenses, and analytical and medical optical instruments, leads to significant image distortion due to the bidirectional dependence of the transmission light.

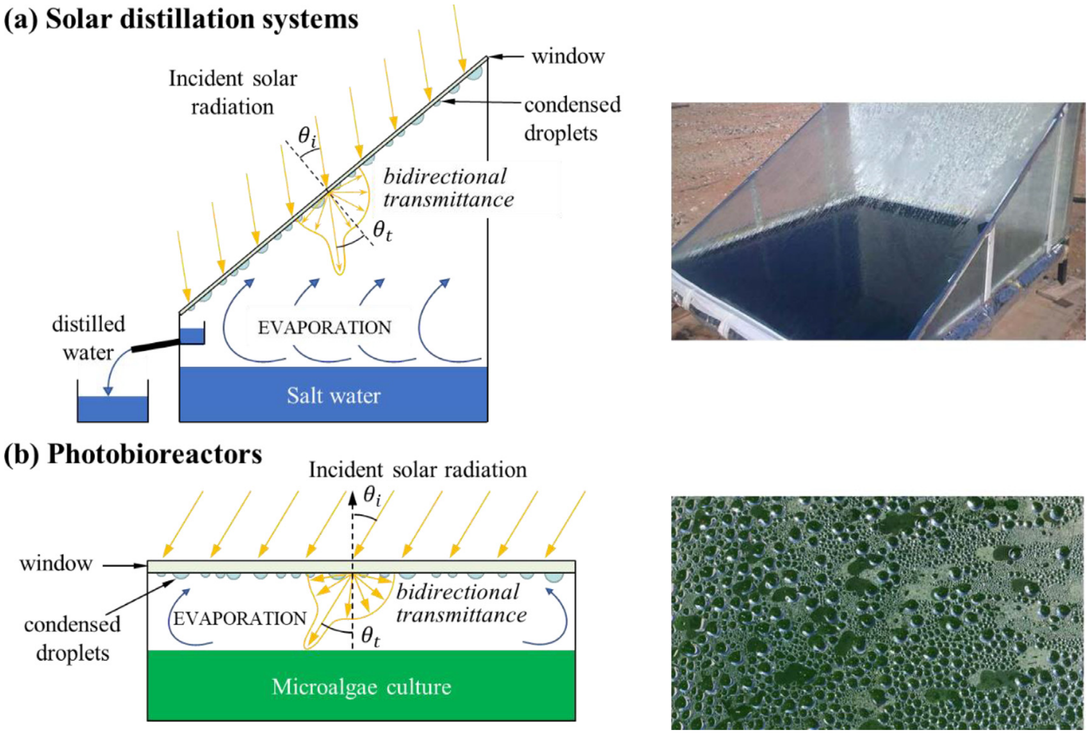

Fig. 1. Schematic of effects of the bidirectional transmittance on (a) the solar distillation system, (b) the photobioreactors. Photograph of Fig. 1(a) courtesy of V-EnerTek, Chennai, India, Used by permission. All rights reserved. © 2020 V-EnerTek. The photograph of Fig. 1(b) was taken with permission in the microalgae R&D facility AlgoSolis of the University of Nantes, France (http://algosolis.com/).

Here, the bidirectional transmittance can be used to evaluate the image distortion and possibly reconstruct the images [37].

Pollet and Pieters [30] investigated experimentally forward scattering by backside droplets on a single vertical glass pane described by the bidirectional transmittance as a function of the phase of the condensation process, the wavelength of light, and the incident angle. The authors found that more than 80% of the transmitted visible radiation was scattered due to the condensate. They also measured the bidirectional transmittance of four different transmitting materials, namely single glass, low density polyethylene, anti-drop condensation polyethylene and diffuse polyethylene either dry or covered with condensate [31]. The forward diffusion pattern of the four materials, except anti-drop condensation polyethylene, was broadened by the presence of the droplets. Unfortunately, contact angle and surface area coverage were not reported and their effects on the bidirectional transmittance were not discussed. Lee et al. [24] developed a zwitter-wettable surface coating to explore experimentally their antifogging performance by real-time monitoring of transmittance and image distortion in the visible under collimated and normally incident light and extreme fogging conditions. The results revealed that the new coating maintained high transmission levels and low image distortion. However, the surface coverage and the droplet size distribution were not reported and the effects of incident angle on the transmittance and image distortion were not investigated.

Previous studies have focused on predicting or measuring transmittance under normal incidence and/or considered the overall energy reflected and transmitted by windows supporting nonabsorbing or absorbing droplets on their front side [25] or backside [27,29]. No consideration was given to the bidirectional nature of the transmittance and how it might differ when droplets are present on the front or on the back side of windows. The present study aims to investigate systematically the bidirectional transmittance of transparent windows supporting nonabsorbing cap-shaped droplets on their front side or backside. Particular attention was paid to the effects of droplet size distribution, contact angle, surface area coverage, as well as incident polar and azimuthal angles. The results are relevant to recent advances in materials and surface coatings developed to mitigate the visibility reduction and image distortion of optical windows caused by the presence of droplets. They can also be used in 3D computer graphics and 3D rendering for animations, video games, and virtual reality.

2. Analysis

2.1. Problem statement

Fig. 2 schematically illustrates the problem under investigation focusing on light transfer through transparent windows exposed to collimated incident radiation and supporting nonabsorbing cap-shaped droplets on the (a) front side or (b) backside, and (c) the top view of the transparent window supporting polydisperse droplets. A plane parallel window with length L, width W, and thickness H was exposed to collimated light incident on its front side at a polar angle θ_i. Monodisperse or polydisperse droplets were randomly distributed on the front side or backside of the window. Droplets were assumed to be cap-shaped with constant curvature, contact angle θ_c, and diameter d much smaller than the capillary length l_c. For water droplets in air, the capillary length l_c is 2.7 mm [39]. Therefore, the droplet diameter d was smaller than 270 μm to satisfy $d \ll l_c$. Under these conditions, the shape of the droplet is controlled by surface tension. In addition, the dynamics of condensation and the associated changes in droplet size were ignored by virtue of the fact that (i) light transfer takes place at speed much faster than any heat or mass transfer processes and (ii) visible light transfer is decoupled from the heat and mass transfer as it does not contribute to radiative heat transfer. The incident light was reflected or transmitted by the transpar-

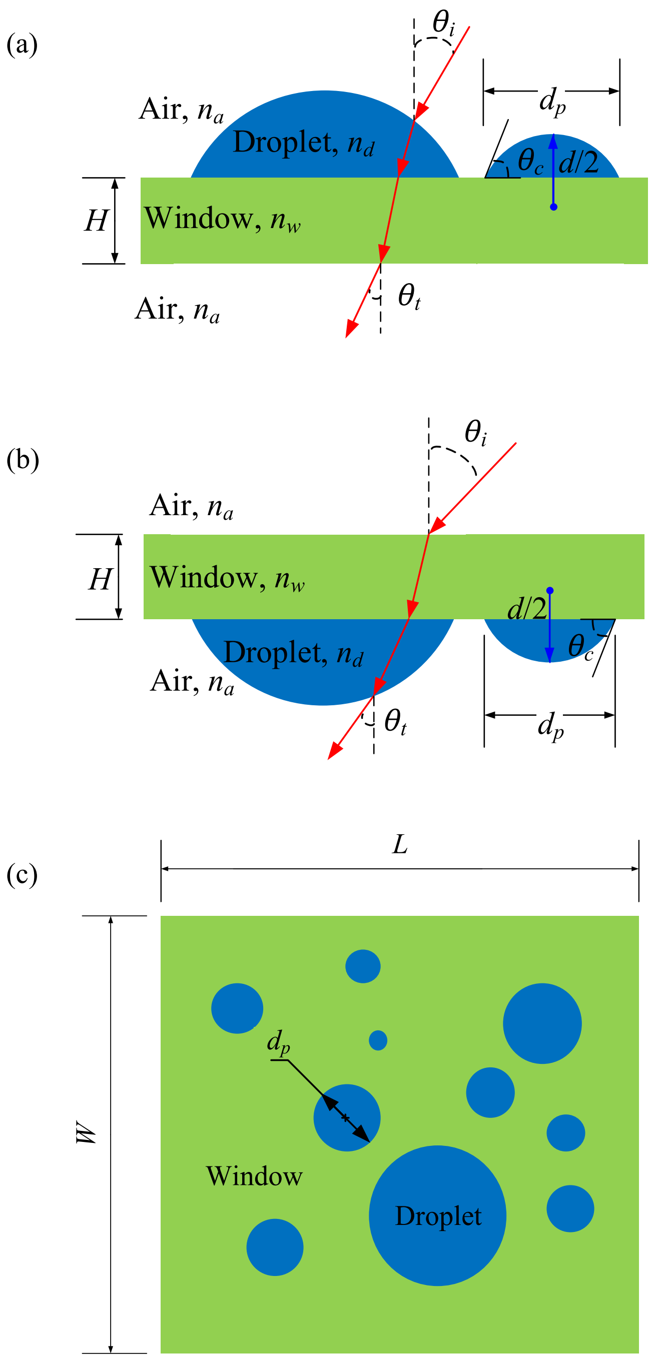

Fig. 2. Schematic of light transfer through transparent windows with nonabsorbing cap-shaped droplets (a) on the front face or (b) on the backside. (c) Projected view of the transparent window supporting polydisperse droplets.

ent windows or by the nonabsorbing droplets with refractive index denoted by n_w and n_d, respectively. Then, light could be transmitted through the backside of the windows (Fig. 2a) or through the droplets (Fig. 2b) at a transmission angle θ_t. In the present study, the dimensions of the windows were taken as $L = W = 5.0$ mm, and $H = 3.0$ mm. The refractive indices of the surrounding air, windows, and droplets were taken respectively as $n_a = 1.0$, $n_w = 1.5$, and $n_d = 1.33$ corresponding to the visible part of the solar spectrum. Here, the projected surface area coverage f_A was defined based on the projected diameter d_p such that $d_p = d \sin[\min(\theta_c, 90°)]$ [26].

3. Methods

Droplets were generated numerically by using the same methodology used in our previous studies [25,26,29] and described in details in Ref. [26]. In brief, droplets were placed randomly in a square domain representing the window surface and were either monodisperse or polydisperse with size distribution following a uniform distribution [40]. To make the problem mathematically tractable, the same assumptions as in Refs. [25,26,29] were made here. In brief, all interfaces were optically smooth and Snell's law and Fresnel's equations were valid. The dimensions of the droplets and window were much larger than the wavelength of the incident light so geometric optics prevailed and inelastic scattering, interferences, and other wave effects could be ignored. The window and droplets were nonabsorbing and had constant and uniform refractive indices. Similarly, Monte Carlo ray-tracing method [41,42] was used to predict light transfer through the windows supporting droplets. The boundary conditions on the sides of the simulation domain were periodic in order to avoid boundary effects, i.e., both the window and droplets were assumed periodic. These boundary conditions were described in detail in Refs. [26,29] and need not be repeated.

In this paper, two situations were considered in computing the bidirectional transmittance in order to analyze separately the effects of incident polar angle θ_i and azimuthal angle φ_i. First, we focused on the effect of incident polar angle θ_i on the one-dimensional bidirectional transmittance averaged over the incident azimuthal angle φ_i. For this purpose, Monte Carlo ray tracing method launched photons with a random azimuthal angle φ_i. Then, the one-dimensional bidirectional transmittance was calculated according to [41,42]

$$\overline{T}_{bd}(\theta_i, \theta_t) = \frac{N_t}{N_i\, 2\pi\ \cos\theta_t\ \sin\theta_t \Delta\theta_t}, \tag{1}$$

where N_i is the total number of incident rays and N_t is the number of transmission rays in the elementary solid angle $\Delta\Omega_t = 2\pi$ $\sin\theta_t\ \Delta\theta_t$. Here, the transmission angle θ_t ranging from 0 to 90° was divided into $M + 1$ intervals, with $\Delta\theta_t = \pi/(4M)$ (in rad) for the first and last intervals at angles $\theta_t = \pi/(8M)$ (in rad) and $\pi/2 - \pi/(8M)$ (in rad) while the interval $\Delta\theta_t = \pi/(2M)$ (in rad) was uniform for other transmission angles θ_t. In order to achieve numerical convergence for the predicted bidirectional transmittance, the total number of incident rays was $N_i = 10^7$ and the number of transmission angle intervals was $M = 90$.

Second, the effect of incident azimuthal angle φ_i was considered. In the simulations, a specific azimuthal angle φ_i was arbitrarily chosen. Thus, the bidirectional transmittance could be expressed as [41,42]

$$T_{bd}(\theta_i, \varphi_i, \theta_t, \varphi_t) = \frac{N_t}{N_i \cos\theta_t\ \sin\theta_t \Delta\theta_t \Delta\varphi_t}, \tag{2}$$

where N_t was the number of transmission rays in the solid angle $\Delta\Omega_t = \sin\theta_t\ \Delta\theta_t\ \Delta\varphi_t$. In order to achieve numerical convergence for the predicted bidirectional transmittance, the total number of incident photons was taken as $N_t = 10^7$ and the azimuthal angle of the transmission was divided into 360 intervals, i.e., $\Delta\varphi_t = \pi/180$ (in rad) while the discretization in the polar angle $\Delta\theta_t$ was the same as that mentioned previously. Note that, due to the symmetry of the cap-shaped droplets, the bidirectional transmittance given by Eq. (2) satisfied $T_{bd}(\theta_i, \varphi_i, \theta_t, \varphi_t) = T_{bd}(\theta_i, \theta_t, \varphi_t - \varphi_i)$. Therefore, the relationship between the one-dimensional bidirectional transmittance $\overline{T}_{bd}(\theta_i, \theta_t)$ and the bidirectional transmittance $T_{bd}(\theta_i, \varphi_i, \theta_t, \varphi_t)$ given by Eqs. (1) and (2) can be expressed as

$$\overline{T}_{\text{bd}}(\theta_i,\ \theta_t) = \frac{1}{2\pi}\int_0^{2\pi}\frac{1}{2\pi}\int_0^{2\pi} T_{\text{bd}}(\theta_i,\ \varphi_i,\ \theta_t,\ \varphi_t)\ \text{d}\varphi_t\text{d}\varphi_i$$
$$= \frac{1}{2\pi}\int_0^{2\pi} T_{\text{bd}}(\theta_i,\ \varphi_i,\ \theta_t,\ \varphi_t)\ \text{d}\varphi_t. \quad (3)$$

Similarly, these bidirectional transmittances are related to the one-dimensional directional-hemispherical transmittance $\overline{T}_{\text{dh}}(\theta_i)$ previously investigated for droplets on the front and back sides of window [25,26,29] according to

$$\overline{T}_{\text{dh}}(\theta_i) = 2\pi\int_0^{\pi/2}\overline{T}_{\text{bd}}(\theta_i,\ \theta_t)\cos\theta_t\ \sin\theta_t\ \text{d}\theta_t$$
$$= \int_0^{2\pi}\int_0^{\pi/2} T_{\text{bd}}(\theta_i,\ \varphi_i,\ \theta_t,\ \varphi_t)\cos\theta_t\ \sin\theta_t\ \text{d}\theta_t\text{d}\varphi_t. \quad (4)$$

4. Results and discussion

This section presents a parametric study investigating the effects of (i) droplet size distributions and (ii) contact angle θ_c, (iii) incident polar θ_i and azimuthal φ_i angles, and (iv) projected surface area coverage f_A on the bidirectional transmittance of transparent windows with nonabsorbing droplets either on their front side or backside.

4.1. Effects of droplet size distribution and incident polar angle

Fig. 3 plots the one-dimensional bidirectional transmittance $\overline{T}_{\text{bd}}(\theta_i,\ \theta_t)$ of windows supporting randomly distributed monodisperse or polydisperse nonabsorbing droplets (a) on their front side and (b) on their backside for contact angle $\theta_c = 90°$ and projected surface area coverage $f_A = 50\%$ as a function of transmission angle θ_t for different droplet size distribution and incident angle θ_i. Three droplet size distributions were considered namely (i) monodisperse droplets with $d_m = 100$ μm, (ii) monodisperse droplets with $d_m = 250$ μm, and (iii) polydisperse droplets following a normal distribution with $d_m = 100$ μm and standard deviation $\sigma = d_m/2 = 50$ μm such that the droplet diameter d satisfied $d_m - \sigma < d < d_m + \sigma$. Fig. 3 indicates that the one-dimensional bidirectional transmittance of windows, with nonabsorbing droplets on either sides, was independent of droplet size distribution (monodisperse or polydisperse) and of the droplet mean diameter for given contact angle θ_c and surface area coverage f_A. These results were consistent with our previous studies focusing on the one-dimensional directional-hemispherical transmittance $\overline{T}_{\text{dh}}(\theta_i)$ [25,26]. Thus, the results presented in the remaining of this paper were obtained for monodisperse and randomly distributed droplets with diameter $d_m = 100$ μm.

Moreover, comparing Figs. 3(a) and 3(b) establishes that the one-dimensional bidirectional transmittance $\overline{T}_{\text{bd}}(\theta_i,\ \theta_t)$ is significantly different if the droplets are present on the front side or on the back side of the window, as discussed extensively in the following section. However, in both cases, $\overline{T}_{\text{bd}}(\theta_i,\ \theta_t)$ had a sharp peak at the incident direction $\theta_t = \theta_i$ corresponding to the transmitted photons that had not interacted with the droplets. In addition, the one-dimensional normal-directional transmittance $\overline{T}_{\text{bd}}(\theta_i = 0°,\ \theta_t)$ decreased nearly monotonously with increasing transmission angle, while the transmission energy for other incident angles $\theta_i = 30°$ and $60°$ was more distributed over all transmission angles. This can be attributed to the fact that the photons with oblique incidence experienced multiple internal reflections between the two faces of the window and were more likely to enter into the droplets and be transmitted (or reflected) in different directions compared to when the photons were normally incident.

4.2. Effects of contact angle

4.2.1. Droplets on window's front side

Fig. 4 shows (a) the one-dimensional normal-directional transmittance $\overline{T}_{\text{bd}}(\theta_i = 0°,\ \theta_t)$ for different contact angle θ_c between 30° and 180° and (b) the one-dimensional bidirectional transmittance $\overline{T}_{\text{bd}}(\theta_i,\ \theta_t)$ at $\theta_i = 0°$, 30°, and 60° for contact angle $\theta_c = 45°$, as functions of transmission angle θ_t. In all cases, the window supported nonabsorbing, monodisperse, and randomly distributed droplets on its front side with $d_m = 100$ μm and projected surface coverage $f_A = 50\%$. Fig. 4(a) indicates that, for droplets with contact angle $\theta_c < 90°$, the one-dimensional normal-directional transmittance $\overline{T}_{\text{bd}}(\theta_i = 0°,\ \theta_t)$ featured a cutoff transmission angle beyond which it decreased sharply, by several orders of magnitude. The cutoff angle, denoted by $\theta_{t,\text{co}}^{E,+}$, was larger than the transmission angle $\theta_t = \theta_i$ corresponding to the sharp peak. It is also interesting to note that the cutoff angle $\theta_{t,\text{co}}^{E,+}$ increased with increasing contact angle. However, no cutoff angle was observed in one-dimensional the normal-directional transmittance for contact angle $\theta_c > 90°$.

Moreover, Fig. 4(b) indicates that, for contact angle $\theta_c = 45°$ and incident angle $\theta_i = 30°$, the one-dimensional bidirectional transmittance $\overline{T}_{\text{bd}}(\theta_i,\ \theta_t)$ featured both large and small cutoff transmission angles $\theta_{t,\text{co}}^{E,+}$ and $\theta_{t,\text{co}}^{E,-}$, which were larger and smaller than the transmission angle $\theta_t = \theta_i$, respectively. However, neither $\theta_{t,\text{co}}^{E,+}$ nor $\theta_{t,\text{co}}^{E,-}$ existed in the one-dimensional bidirectional transmittance for incident angle $\theta_i = 60°$. Finally, note that the oscillations in transmittance, observed in Fig. 4(a) ($\theta_c = 30°$, $\theta_t \geq 10°$) and in Fig. 4(b) ($\theta_i = 0°$, $\theta_t \geq 20°$), were due to the numerical noise and to very small values of transmittance.

Fig. 5 schematically illustrates the cutoff transmission angles $\theta_{t,\text{co}}^{E,+}$ and $\theta_{t,\text{co}}^{E,-}$ in the one-dimensional bidirectional transmittance $\overline{T}_{\text{bd}}(\theta_i,\ \theta_t)$ of a window with external droplets and their relationships to the contact angle θ_c and incident angle θ_i. Fig. 5(a) features collimated rays obliquely incident on a droplet or on the dry window with an incident angle θ_i corresponding to an incident angle θ_i' defined with respect to the normal of the air/droplet interface. The local normal of the air/droplet interface forms an angle θ_n with the normal to the window such that $\theta_i' = \theta_n - \theta_i$ when $\theta_i \leq \theta_n$ [Fig. 5(a)] and $\theta_i' = \theta_i - \theta_n$ when $\theta_i > \theta_n$, i.e., $\theta_i' = |\theta_n - \theta_i|$. Most rays were transmitted across the air/droplet interface into the droplet with transmission angle θ_t' and then were incident on the droplet/window interface with incident angle θ_i''. Finally, the rays were transmitted through the droplet/window interface with transmission angle θ_t'' to eventually emerge on the other side of the plane parallel window with transmission angle θ_t. The latter can be determined according to Snell's law and geometric considerations at the different interfaces such that

$$n_a \sin\theta_i' = n_d \sin\theta_t' \quad (5)$$

and

$$n_d \sin\theta_i'' = n_w \sin\theta_t'' = n_a \sin\theta_t. \quad (6)$$

Here, $\theta_i'' = \theta_n - \text{sign}(\theta_n - \theta_i)\theta_t'$, as shown in Fig. 5(a). In the limiting case when rays are incident on the contact line of the droplets then $\theta_n = \theta_c$. This situation corresponds to the cutoff transmission angle $\theta_{t,\text{co}}^{E,+}$ shown in Fig. 4. For contact angle $\theta_c \leq 90°$, Eqs. (5) and (6) can be combined to express the cutoff transmission angle $\theta_{t,\text{co}}^{E,+}$ as

$$\theta_{t,\text{co}}^{E,+} = \sin^{-1}\left\{n_d/n_a\sin\left[\theta_c + \sin^{-1}(n_a/n_d\sin(\theta_i - \theta_c))\right]\right\}. \quad (7)$$

Considering the case of normal incidence with $n_a = 1.0$ and $n_d = 1.33$, the large cutoff angle $\theta_{t,\text{co}}^{E,+}$ of $\overline{T}_{\text{bd}}(\theta_i,\ \theta_t)$ is equal to 10.6°, 26.2° and 61.3° for contact angle $\theta_c = 30°$, 60° and 90°, respectively. These predictions were in excellent agreement with

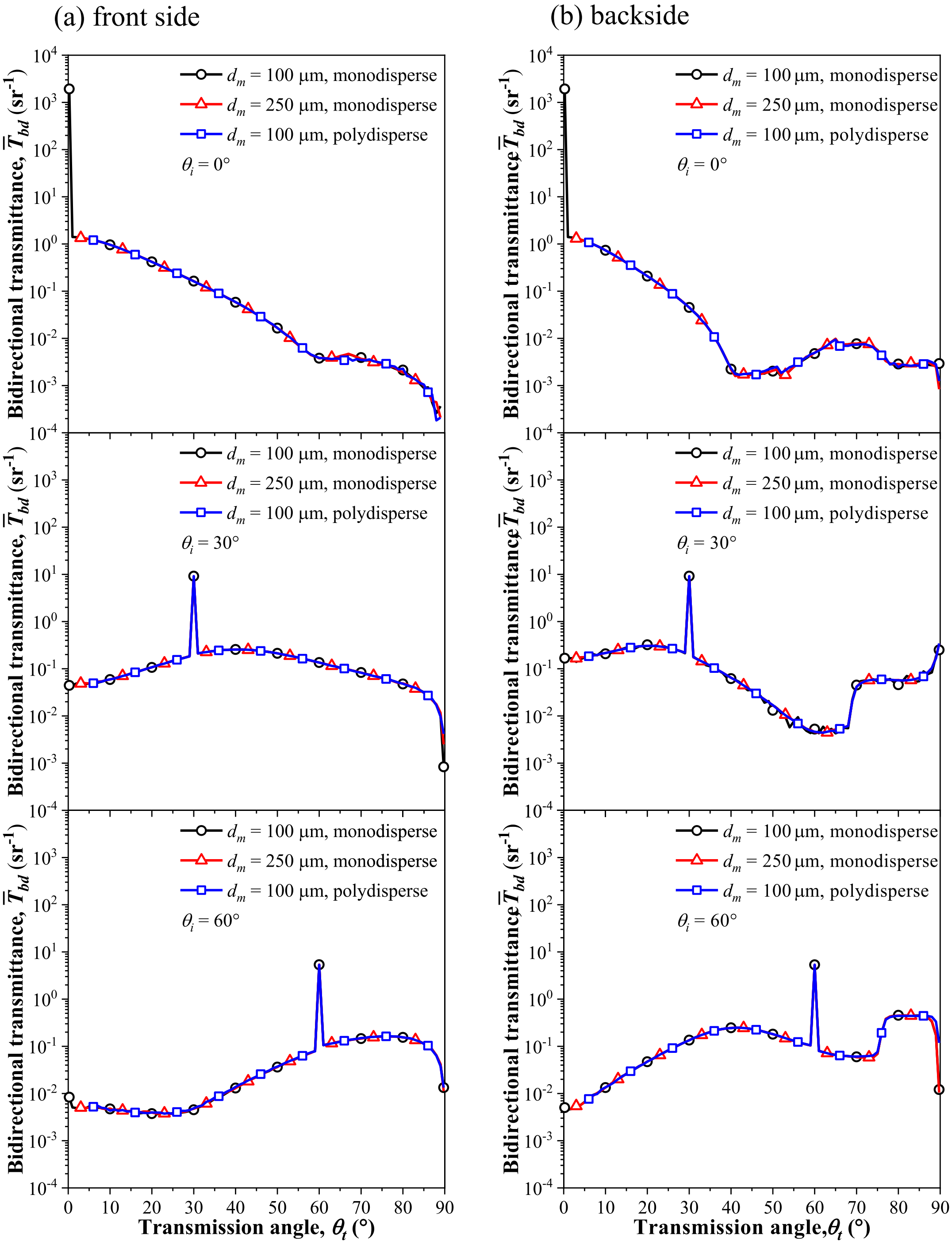

Fig. 3. One-dimensional bidirectional transmittance $\overline{T}_{\mathrm{bd}}(\theta_i, \theta_t)$ as a function of transmission angle for different size distributions of droplets and incident angles. The window supported monodisperse or polydisperse and randomly distributed droplets either (a) on its front side or (b) on its backside for $\theta_c = 90°$ and $f_A = 50\%$. The diameter of polydisperse droplets followed a normal distribution and was such that $d_m - \sigma < d < d_m + \sigma$ with $d_m = 100$ μm and $\sigma = d_m/2 = 50$ μm.

our numerical simulations, as illustrated in Fig. 4(a). Moreover, the cutoff angle $\theta_{t,\mathrm{co}}^{E,+}$ of $\overline{T}_{\mathrm{bd}}(\theta_i,\ \theta_t)$ was equal to 17.2° and 47.7° for $\theta_c = 45°$, $\theta_i = 0°$ and $\theta_c = 45°$, $\theta_i = 30°$, respectively. Here also, excellent agreement was observed between numerical simulations [Fig. 4(b)] and predictions by Eq. (7). Note that to ensure that Eq. (7) is valid, the condition $\theta_c + \sin^{-1}[n_a/n_d\ \sin(\theta_i - \theta_c)] \leq \theta_{cr}$ should be satisfied, where the critical angle for total internal reflection $\theta_{cr} = \sin^{-1}(n_a/n_d) = 48.8°$ for $n_a = 1.0$ and $n_d = 1.33$. Otherwise, total internal reflection through the window occurs at the backside window/air interface. Then, the conditions on the incident angle θ_i and contact angle θ_c ensuring the existence of the cutoff angle $\theta_{t,\mathrm{co}}^{E,+}$ can be expressed as

$$n_a \sin(\theta_i - \theta_c) \leq n_d \sin(\theta_{\mathrm{cr}} - \theta_c). \tag{8}$$

Here, for $\theta_c = 45°$ and $\theta_i = 60°$, Eq. (8) is not satisfied so that no large cutoff angle $\theta_{t,\mathrm{co}}^{E,+}$ was not observed in Fig. 4(b).

Similarly, Fig. 5(b) shows collimated rays incident on the second part of the droplet such that $\theta_n = \theta_i' - \theta_i$. Eqs. (5) and (6) also prevail but are such that $\theta_i' = \theta_i + \theta_n$ and $\theta_i'' = \theta_t' - \theta_n$. the small cutoff angle $\theta_{t,\mathrm{co}}^{E,-}$ illustrated in Fig. 5(b) corresponds to the limiting

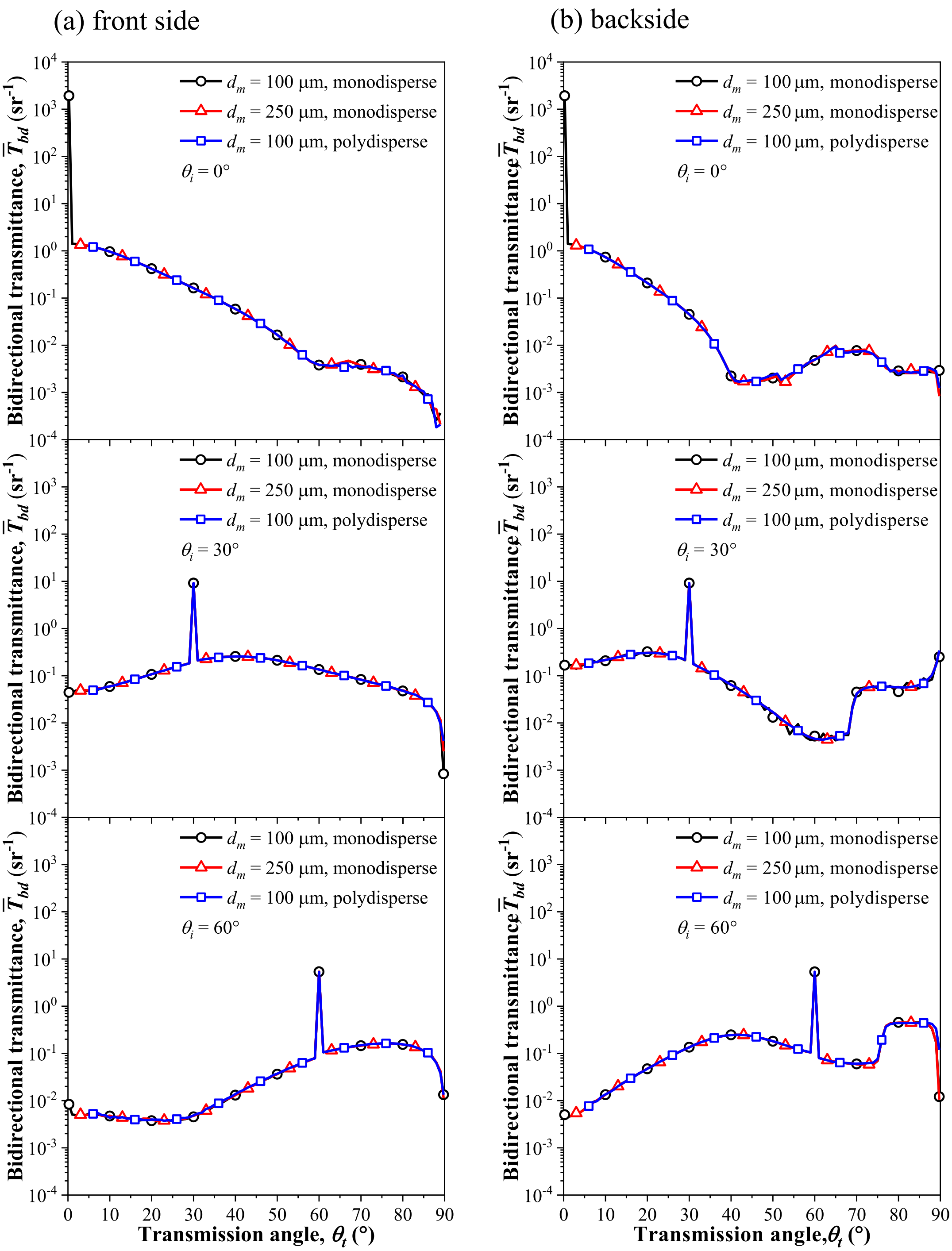

Fig. 4. (a) One-dimensional normal-directional transmittance $\overline{T}_{\text{bd}}(\theta_i = 0^\circ, \theta_t)$ for different values of contact angle θ_c and (b) the one-dimensional bidirectional transmittance $\overline{T}_{\text{bd}}(\theta_i, \theta_t)$ at $\theta_i = 0°$, 30°, and 60° for contact angle $\theta_c = 45°$ as a function of transmission angle. The window supported nonabsorbing, monodisperse, and randomly distributed droplets on its front side with $d_m = 100\ \mu$m and projected surface area coverage $f_A = 50\%$.

case when the rays are incident on the contact line of the droplets, i.e., when $\theta_n = \theta_c$. Then, $\theta_{t,\text{co}}^{E,-}$ can be expressed as

$$\theta_{t,\text{co}}^{E,-} = \sin^{-1}\left\{n_d/n_a \sin\left[\sin^{-1}(n_a/n_d \sin(\theta_c + \theta_i)) - \theta_c\right]\right\}. \tag{9}$$

It was equal to $\theta_{t,\text{co}}^{E,-} = 2.1°$ for $\theta_c = 45°$ and $\theta_i = 30°$ with $n_a = 1.0$ and $n_d = 1.33$. This prediction agrees very well with numerical predictions shown in Fig. 4(b). Here also, the conditions on the incident angle θ_i and contact angle θ_c corresponding to the presence of the small cutoff angle $\theta_{t,\text{co}}^{E,-}$ can be derived as

$$\theta_i + \theta_c \leq 90^\circ \text{ and } n_a \sin(\theta_i + \theta_c) \geq n_d \sin\theta_c. \tag{10}$$

These conditions explains why no small cutoff angle $\theta_{t,\text{co}}^{E,-}$ was observed in the one-dimensional bidirectional transmittance for $\theta_c = 45°$ and $\theta_i = 60°$ [Fig. 4(b)].

Fig. 6 plots the contours and magnitude (a) of the large cutoff angle $\theta_{t,\text{co}}^{E,+}$ and (b) of the small cutoff angle $\theta_{t,\text{co}}^{E,-}$ of the one-dimensional bidirectional transmittance $\overline{T}_{\text{bd}}(\theta_i,\ \theta_t)$ of the window with external droplets as functions of incident angle θ_i and contact angle θ_c based on Eqs. (7) and (9), respectively. Fig. 6(a) illustrates that the large cutoff angle $\theta_{t,\text{co}}^{E,+}$ existed only in the region of the $(\theta_i,\ \theta_c)$ plane where the conditions of Eq. (8) prevailed. It

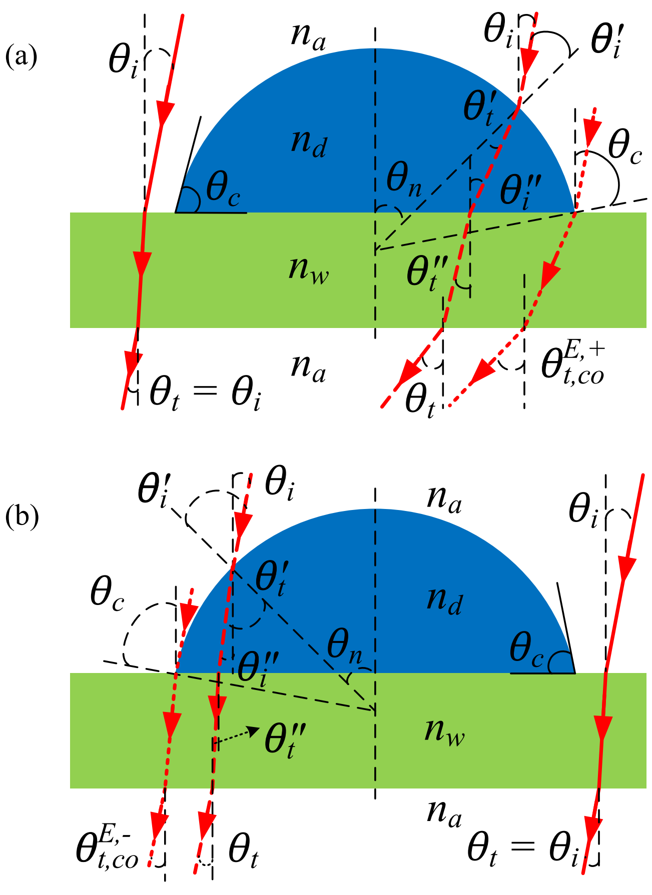

Fig. 5. Schematic illustrating the effect of droplet contact angle θ_c and incident angle θ_i on (a) the large cutoff transmission angle $\theta^{E,+}_{t,co}$ and (b) small cutoff transmission angle $\theta^{E,-}_{t,co}$ of the one-dimensional bidirectional transmittance for external droplets.

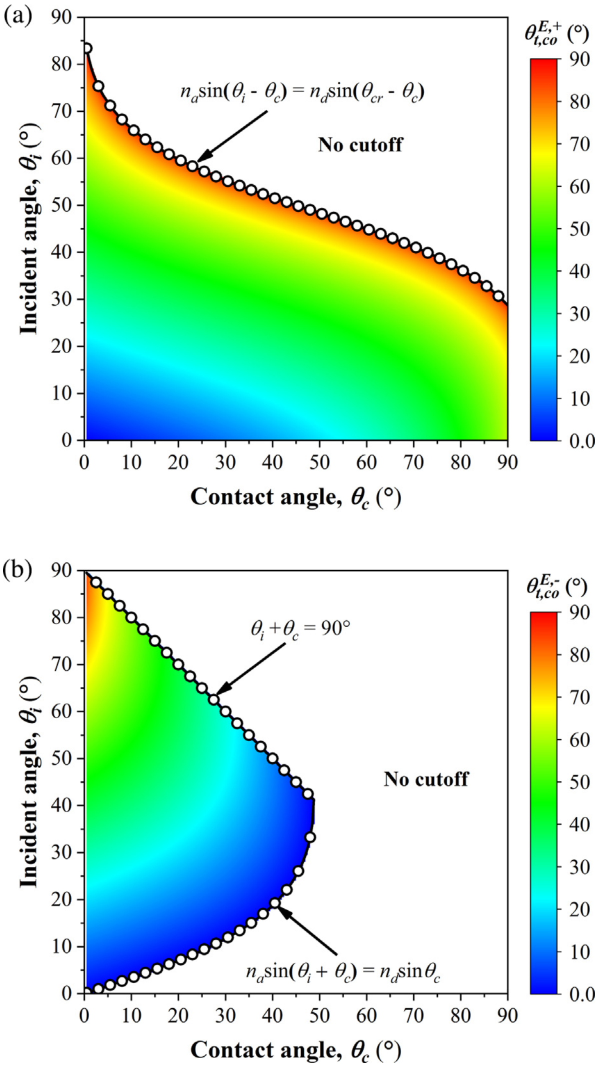

Fig. 6. Contours and magnitude of cutoff transmission angles, (a) $\theta^{E,+}_{t,co}$ and (b) $\theta^{E,-}_{t,co}$, as functions of incident angle θ_i and contact angle θ_c based on Eqs. (6) and (8), respectively.

also indicates that the cutoff angle $\theta^{E,+}_{t,co}$ increased with increasing incident angle θ_i and contact angle θ_c. By contrast, Fig. 6(b) indicates that, the cutoff angle $\theta^{E,-}_{t,co}$ existing in the region bounded by Eq. (10), increased with increasing incident angle θ_i and decreased with increasing contact angle θ_c.

4.2.2. Droplets on window's backside

Fig. 7 shows (a) the one-dimensional normal-directional transmittance $\overline{T}_{\text{bd}}(\theta_i = 0°, \theta_t)$ for different contact angles θ_c between 30° and 180° and (b) the one-dimensional bidirectional transmittance $\overline{T}_{\text{bd}}(\theta_i, \theta_t)$ (θ_i = 0°, 30°, and 60°) for contact angle $\theta_c = 45°$ as functions of transmission angle θ_t. In all cases, the droplets were monodisperse and randomly distributed on the window's backside with $d_m = 100$ μm and projected surface coverage $f_A = 50\%$. Here also, oscillations in $\overline{T}_{\text{bd}}(\theta_i = 0°, \theta_t)$ appeared in Fig. 7(a) ($\theta_c = 30°$, $\theta_t \geq 10°$) and in Fig. 7(b) ($\theta_c = 45°$, $\theta_t \geq 25°$) due to numerical uncertainty and very small transmittance values for $\theta_t > 10°$ and θ_c =30°. Fig. 7 indicates that the larger the droplet contact angle θ_c, the more diffuse the transmittance. In addition, the one-dimensional normal-directional transmittance $\overline{T}_{\text{bd}}(\theta_i = 0°, \theta_t)$ featured a large cutoff angle $\theta^{B,+}_{t,co}$ for droplets located on the window's backside with contact angle θ_c = 30° and 45°. Furthermore, for contact angles such that $\theta_{cr} < \theta_c < 90°$ and under normal incidence [Fig. 7(a)], $\overline{T}_{\text{bd}}(\theta_i = 0°, \theta_t)$ reached a minimum at the transmission angle given by $\theta^B_{t,\min} = 90° - \theta_{cr}$. Here, the critical angle for total internal reflection at the droplet/air interface θ_{cr} was equal to 48.8° so that $\theta^B_{t,\min} = 41.2°$. Moreover, Fig. 7(b) indicates that the small cutoff angle $\theta^{B,-}_{t,co}$ can be observed for contact angle $\theta_c = 45°$ and incident angle $\theta_i = 30°$ or 60°.

Fig. 8 illustrates how inclined rays incident on the window with an incident angle θ_i are refracted and transmitted through the window, or into droplets with incident angle θ_i' and refraction angle θ_t' at the window/droplet interface, and finally through droplets with transmission angle θ_t. The incident angle and refraction angle at the droplet/air interface were denoted by θ_i'' and θ_t''. The transmission angle θ_t could be obtained from Snell's law expressed at each interface as

$$n_a \sin\theta_i = n_w \sin\theta_i' = n_d \sin\theta_t' \tag{11}$$

and

$$n_d \sin\theta_i'' = n_a \sin\theta_t''. \tag{12}$$

Fig. 8(a) illustrates rays traveling through the window and incident near the contact line of droplets. Here, $\theta_i'' = \theta_n + \theta_t'$ and the transmission angle is given by $\theta_t = \theta_t'' - \theta_n$. In the limiting case when the rays through the window are incident on the contact line of the droplets (i.e., when $\theta_n = \theta_c$) the corresponding cutoff trans-

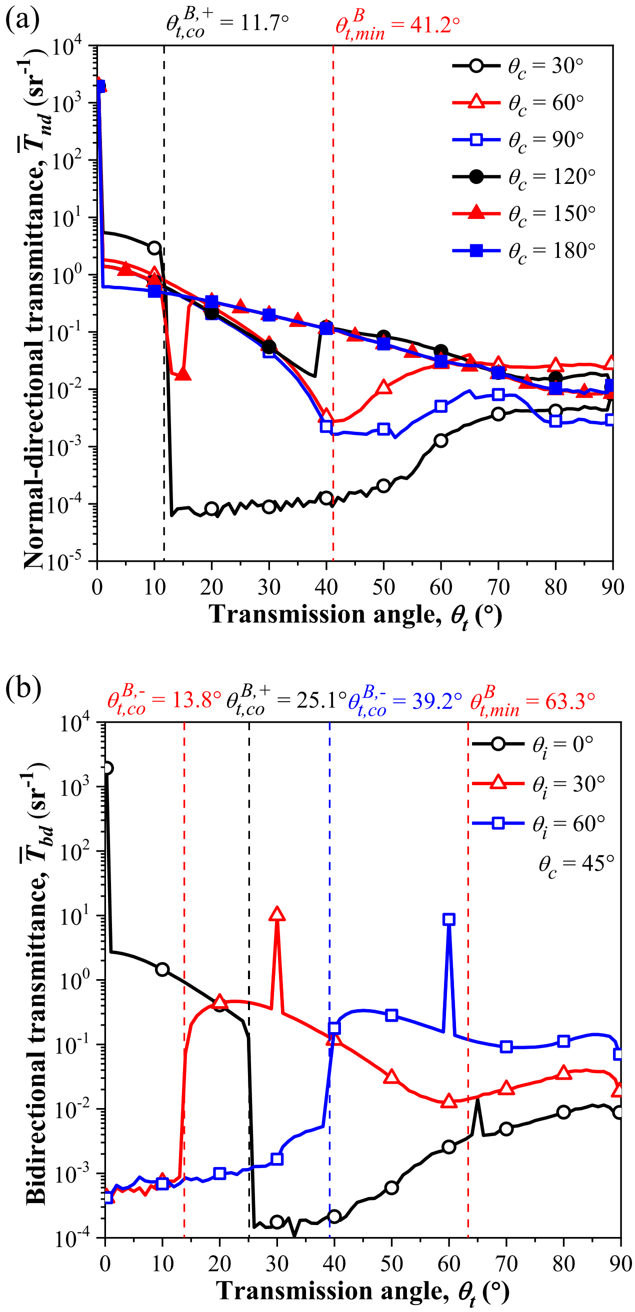

Fig. 7. (a) One-dimensional normal-directional transmittance $\overline{T}_{\text{bd}}(\theta_i = 0^\circ, \theta_t)$ for different values of contact angle θ_c and (b) the one-dimensional bidirectional transmittance $\overline{T}_{\text{bd}}(\theta_i, \theta_t)$ at $\theta_i = 0^\circ$, 30°, and 60°for contact angle $\theta_c = 45^\circ$ as a function of transmission angle. The window supported nonabsorbing, monodisperse, and randomly distributed droplets on its backside with $d_m = 100$ μm and projected surface area coverage $f_A = 50\%$.

mission angle $\theta^{B,+}_{t,\text{co}}$, illustrated in Fig. 8(a), can be expressed as

$$\theta^{B,+}_{t,\text{co}} = \sin^{-1}\left\{n_d/n_a \sin\left[\theta_c + \sin^{-1}(n_a/n_d \sin\theta_i)\right]\right\} - \theta_c. \tag{13}$$

Here, the large cutoff angle $\theta^{B,+}_{t,\text{co}}$ of $\overline{T}_{\text{bd}}(\theta_i = 0^\circ, \theta_t)$ was equal to 11.7° and 25.1° for contact angle θ_c equal to 30° and 45°, respectively. These results were in excellent agreement with the numerical predictions shown in Fig. 7. Note that, in order to avoid total internal reflection at the droplet/air interface and to ensure that Eq. (12) is valid in the limiting case of $\theta_n = \theta_c$, the condition $\theta_i'' = \theta_c + \theta_t' \leq \theta_{cr}$ should be satisfied. According to Eq. (11), $\theta_t' = \sin^{-1}(n_a/n_d \sin\theta_i)$ so that the conditions on the incident angle θ_i and contact angle θ_c to ensure the existence of the large cutoff angle $\theta^{B,+}_{t,\text{co}}$ can be expressed as

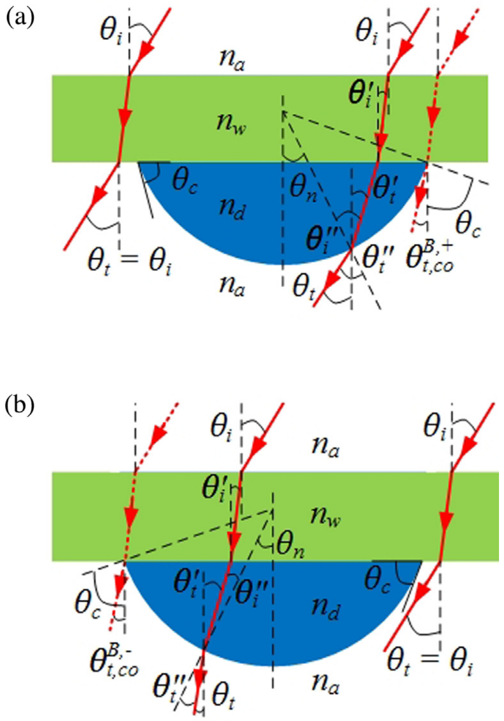

Fig. 8. Schematic illustrating the effect of droplet contact angle and incident angle on (a) the large cutoff transmission angle $\theta^{B,+}_{t,\text{co}}$ and (b) small cutoff transmission angle $\theta^{B,-}_{t,\text{co}}$ of the one-dimensional bidirectional transmittance for backside droplets.

$$n_a \sin\theta_i \leq n_d \sin(\theta_{cr} - \theta_c), \tag{14}$$

where $\theta_c \leq \theta_{cr}$. This is why no large cutoff angles $\theta^{B,+}_{t,\text{co}}$ were observed in the one-dimensional bidirectional transmittance $\overline{T}_{\text{bd}}(\theta_i, \theta_t)$ for $\theta_c = 45^\circ$, $\theta_i = 30^\circ$, and $\theta_i = 60^\circ$ [Fig. 7(b)]. In addition, the one-dimensional bidirectional transmittance $\overline{T}_{\text{bd}}(\theta_i, \theta_t)$ for $\theta_c = 45^\circ$ and $\theta_i = 30^\circ$ featured a minimum around the transmission angle given by $\theta^{B}_{t,\text{min}} = \theta_t'' - \theta_n = \theta_t'' - (\theta_i'' - \theta_t') = 63.3^\circ$ due to total internal reflection at the droplet/air interface, where $\theta_t'' = 90^\circ$, $\theta_t' = \sin^{-1}(n_a/n_d \sin 30^\circ)$, and $\theta_i'' = \theta_{\text{cr}}$.

Similarly, Fig. 8(b) shows oblique rays incident on the opposite side of the droplet near its periphery. Eqs. (11) and (12) also prevail albeit with $\theta_i'' = |\theta_n - \theta_t'|$ and transmission angle expressed as

$$\theta_t = \theta_n - \text{sign}\left(\theta_n - \theta_t'\right)\theta_t''. \tag{15}$$

In the limiting case when the rays were incident on the droplet contact line, then $\theta_n = \theta_c$. The corresponding cutoff transmission angle $\theta^{B,-}_{t,\text{co}}$ illustrated in Fig. 8(b) can be written as

$$\theta^{B,-}_{t,\text{co}} = \theta_c - \sin^{-1}\left\{n_d/n_a \sin\left[\theta_c - \sin^{-1}(n_a/n_d \sin\theta_i)\right]\right\}. \tag{16}$$

The small cutoff angle $\theta^{B,-}_{t,\text{co}}$ of $\overline{T}_{\text{bd}}(\theta_i, \theta_t)$ with droplet contact angle $\theta_c = 45^\circ$ was equal to 13.8° and 39.2° for incident angle θ_i equal to 30° and 60°, respectively. These predictions agreed very well with the numerical simulations reported in Fig. 7(b). Here, $\theta^{B,-}_{t,\text{co}} \geq 0^\circ$ from Eq. (16) so that $\theta_c \geq \sin^{-1}\{n_d/n_a \sin[\theta_c - \sin^{-1}(n_a/n_d \sin\theta_i)]\}$. Therefore, the conditions on the incident angle θ_i and contact angle θ_c ensuring the existence of the small cutoff angle $\theta^{B,-}_{t,\text{co}}$ can be expressed as

$$n_a \sin\theta_i \geq n_d \sin\left[\theta_c - \sin^{-1}(n_a/n_d \sin\theta_c)\right]. \tag{17}$$

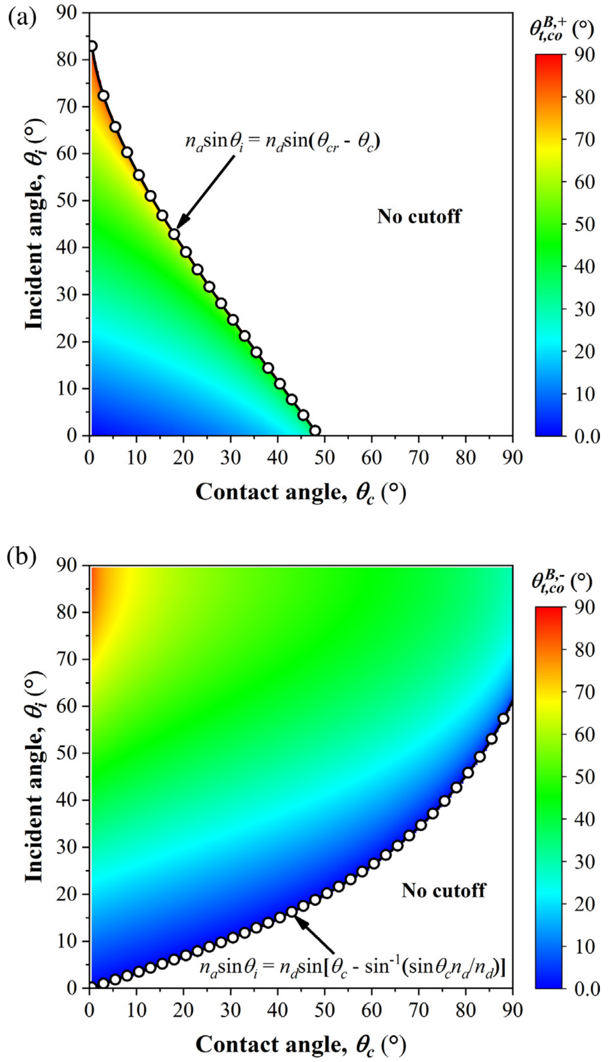

Fig. 9. Contours and magnitude of cutoff transmission angles, (a) $\theta^{B,+}_{t,\mathrm{co}}$ and (b) $\theta^{B,-}_{t,\mathrm{co}}$, as functions of incident angle θ_i and contact angle θ_c based on Eqs. (12) and (15), respectively.

Fig. 9 plots the contours and magnitude (a) of the large cutoff angle $\theta^{B,+}_{t,\mathrm{co}}$ and (b) of the small cutoff angle $\theta^{B,-}_{t,\mathrm{co}}$ of the one-dimensional bidirectional transmittance of a window with backside droplets as functions of incident angle θ_i and contact angle θ_c based on Eqs. (13) and (16). Fig. 9(a) indicates that, the cutoff angle $\theta^{B,+}_{t,\mathrm{co}}$ existed in the region of the (θ_i, θ_c)-plane bounded by Eq. (14) and increased with increasing incident angle θ_i and contact angle θ_c. By contrast, Fig. 9(b) indicates that the cutoff angle $\theta^{B,-}_{t,\mathrm{co}}$ increased with increasing incident angle θ_i and decreased with increasing contact angle θ_c. Comparing Figs. 6 and 9 indicates that the large cutoff angle prevailed when the droplets were on the front side, while the small cutoff angle predominated when the droplets were on the backside. This is attributed to the fact that, for external droplets, the photons corresponding to the large cutoff angle were likely to be incident on the contact line of the droplet, compared with photons responsible for the small cutoff angle. By contrast, for droplets on the window backside, the rays corresponding to the small cutoff angle were more likely to be transmitted through the droplets due to the absence of total internal reflection at the droplet/air interface, unlike those responsible for the large cutoff angle.

4.3. Effects of projected surface area coverage

Fig. 10 shows the one-dimensional bidirectional transmittance $\overline{T}_{\mathrm{bd}}(\theta_i, \theta_t)$ of windows with droplets on (a) the front side or (b) backside as a function of transmission angle θ_t for projected surface area coverage f_A equals to 10%, 30%, and 50% and incident angle $\theta_i = 0^{\circ}$, 30°, and 60°. Here also, the droplets were nonabsorbing, monodisperse, and randomly distributed with $\theta_c = 45°$ and $d_m = 100$ μm. Fig. 10 indicates that, regardless whether the droplets were located on the front or backside of the window surface, the one-dimensional bidirectional transmittance $\overline{T}_{\mathrm{bd}}(\theta_i, \theta_t)$ at the transmission angle $\theta_t = \theta_i$ decreased with increasing f_A. However, it increased with increasing surface area coverage f_A at other transmission angles, i.e., $\theta_t \neq \theta_i$. The increase was uniform across the transmission hemisphere and featured the same cutoff transmission angles $(\theta^{B,+}_{t,\mathrm{co}}, \theta^{B,-}_{t,\mathrm{co}})$ or $(\theta^{E,+}_{t,\mathrm{co}}, \theta^{E,-}_{t,\mathrm{co}})$ previously discussed, for all values of f_A considered, provided the conditions for their existence were satisfied. These results could be explained by the fact that the larger the droplet surface coverage f_A the fewer photons were transmitted directly through the dry part of the window. Instead, photons were scattered by the droplets in all transmission directions other than the incident direction. Similar qualitative results were obtained for different droplet contact angles θ_c (see Figs. S1 and S2 in Supplementary Materials).

4.4. Hemispherical distributions of the bidirectional transmittance

Fig. 11 plots the hemispherical distributions of the bidirectional transmittance $T_{bd}(\theta_i, \varphi_i, \theta_t, \varphi_t)$ defined in Eq. (2) for normal incidence ($\theta_i = 0°$) (a) with external droplets and (b) with backside droplets and for incident direction ($\theta_i = 30°$, $\varphi_i = 120°$) (c) with external droplets and (d) backside droplets. In all cases, the windows supported nonabsorbing monodisperse and randomly distributed droplets with $\theta_c = 45°$, $d_m = 100$ μm, and $f_A = 50\%$. First, Figs. 11(a) and 11(b) indicate that the hemispherical distributions of the normal-directional transmittance $T_{bd}(\theta_i = 0°, \varphi_i, \theta_t, \varphi_t)$ were centrosymmetric with respect to the transmission azimuthal angle for either external or backside droplets. In other words, it was independent of the azimuthal angle φ_i. This was due to the central symmetry of cap-shaped droplets considered. Moreover, the normal-directional transmittance for external droplets [Fig. 11(a)] featured the cutoff angle $\theta^{E,+}_{t,\mathrm{co}} = 17.2°$, as previously observed in Fig. 4(b). By contrast, the normal-directional transmittance for backside droplets [Fig. 11(b)] featured the cutoff angle $\theta^{B,+}_{t,\mathrm{co}} = 25.1°$, as also observed in Fig. 7(a).

Moreover, Figs. 11(c) and 11(d) indicate that the hemispherical distributions of the bidirectional transmittance $T_{bd}(\theta_i, \varphi_i, \theta_t, \varphi_t)$ were symmetric with respect to the plane of incidence defined by the incident direction $\mathbf{s_i}$ and the normal to the window $\mathbf{n_w}$. They also indicate that the incident azimuthal angle φ_i affected significantly the hemispherical distribution of the bidirectional transmittance. For example, the bidirectional transmittance $T_{bd}(\theta_i = 30°, \varphi_i = 120°, \theta_t, \varphi_t)$ of windows with external droplets [Fig. 11(c)] was concentrated in the region bounded by the cutoff polar angle which varied with the cutoff azimuthal angle. Here, the maximum and minimum cutoff polar angles located in the plane of incidence were precisely the large cutoff angle $\theta^{E,+}_{t,\mathrm{co}} = 47.7°$ and the small cutoff angle $\theta^{E,-}_{t,\mathrm{co}} = 2.1°$, respectively, as previously illustrated in Fig. 4(b). By contrast, for droplets present on the window's backside [Fig. 11(d)], the bidirectional transmittance $T_{bd}(\theta_i = 30°, \varphi_i = 120°, \theta_t, \varphi_t)$ featured a small cutoff polar angle which varied with the cutoff azimuthal angle. Similarly, the minimum cutoff polar angle located in the plane of incidence was the same as the cutoff angle $\theta^{B,-}_{t,\mathrm{co}} = 13.8°$ illustrated in Fig. 7(b). Note that similar qualitative results were observed for different contact angles θ_c (see Figs. S3 and S4 in Supplementary Materials).

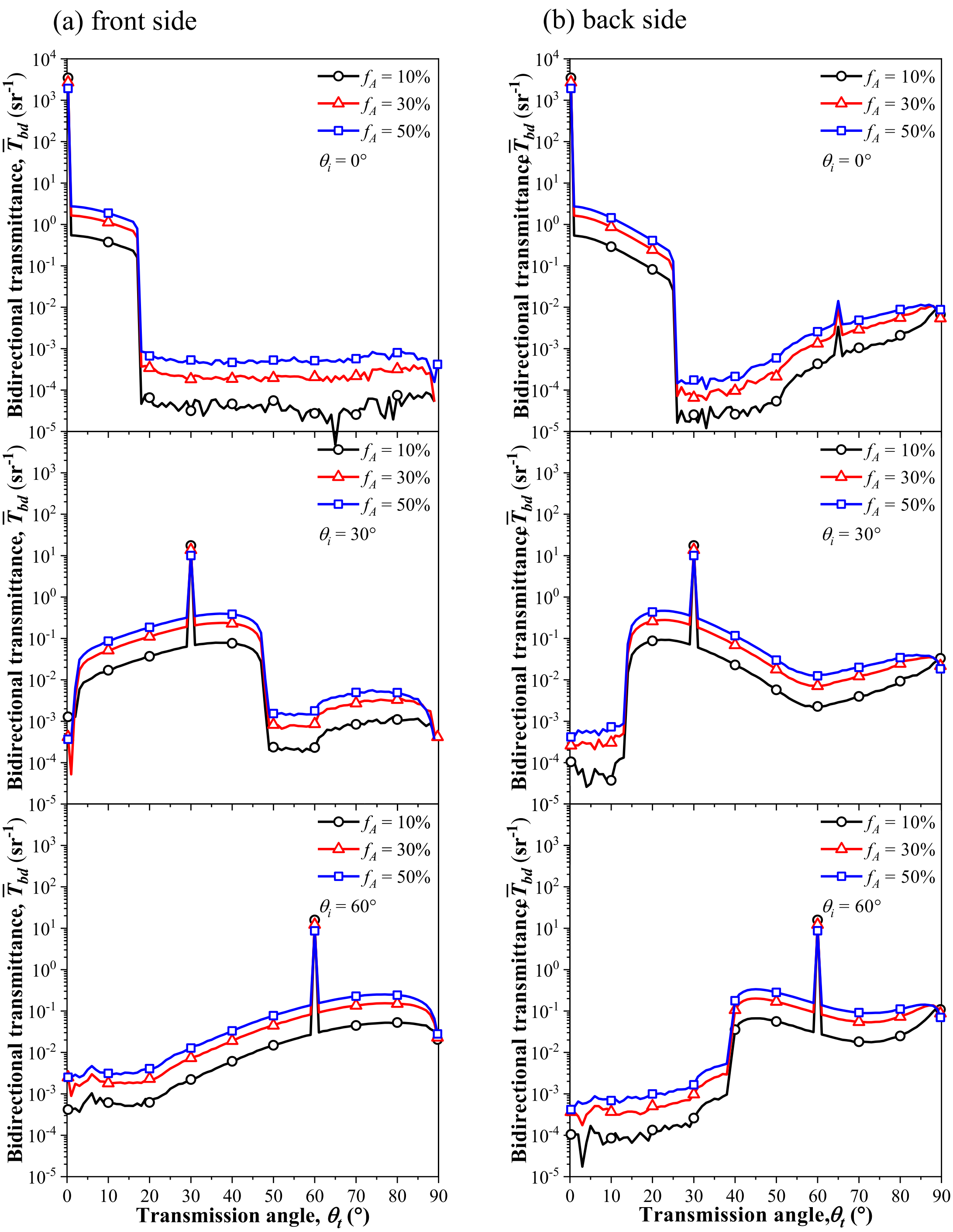

Fig. 10. One-dimensional bidirectional transmittance $\overline{T}_{\mathrm{bd}}(\theta_i, \theta_t)$ as a function of transmission angle for different projected surface area coverage f_A. The window with (a) external condensation or (b) backside condensation supported monodisperse and randomly distributed droplets with θ_c = 90° and d_m = 100 μm.

The relationship between the cutoff polar and azimuthal angles can be predicted by Snell's law. Fig. 12 shows the schematic illustrating the three-dimensional ray propagation through a window with (a) external droplets and (b) backside droplets. Fig. 12(a) illustrates a window with external droplets exposed to collimated rays with an arbitrary polar θ_i and azimuthal φ_i angles incident on the contact line of the droplet. The unit vector of the incident direction $\mathbf{s}_i$ can be expressed as

$$\mathbf{s}_i = [\cos\varphi_i \sin\theta_i, \sin\varphi_i \sin\theta_i, \ -\cos\theta_i]^{\mathrm{T}}. \quad (18)$$

The unit vector of the outer normal on the contact line of the droplet $\mathbf{n}_{d,c,}$ corresponding to the cutoff angle, is defined as

$$\mathbf{n}_{d,c} = [\cos\varphi_{n,c} \sin\theta_{n,c}, \sin\varphi_{n,c} \sin\theta_{n,c}, \cos\theta_{n,c}]^{\mathrm{T}}, \quad (19)$$

where $\theta_{n,c} = \theta_c$ and $\varphi_{n,c} \in [\varphi_i - \pi/2, \varphi_i + 3\pi/2]$. Here, $\varphi_{n,c} \in [\varphi_i - \pi/2, \varphi_i + \pi/2]$ corresponds to the small cutoff angle $\theta_{t,co}^{E,-}$ and $\varphi_{n,c} \in [\varphi_i + \pi/2, \varphi_i + 3\pi/2]$ to the large cutoff angle $\theta_{t,co}^{E,+}$, as illustrated in Fig. 5. Then, based on Snell's law, the unit direction

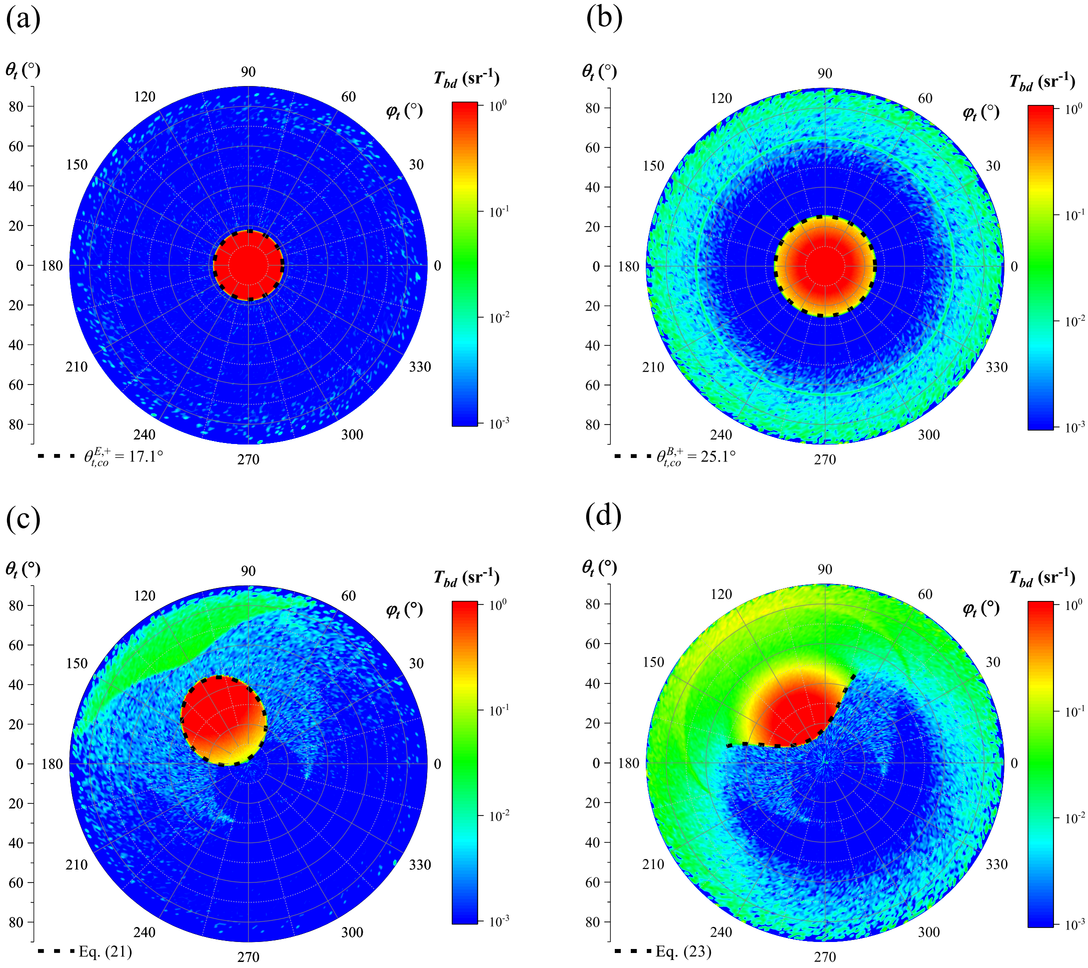

Fig. 11. Hemispherical distributions of the bidirectional transmittance $T_{bd}(\theta_i, \varphi_i, \theta_t, \varphi_t)$ for incident angle of $\theta_i = 0°$ and (a) external droplets and (b) backside droplets, and for incident angle $\theta_i = 30°$, $\varphi_i = 120°$ and (c) external droplets and (d) backside droplets. The window supported monodisperse and randomly distributed droplets with $\theta_c = 45°$, $d_m = 100\ \mu$m, and $f_A = 50\%$.

vector of the ray transmitted in the droplet $\mathbf{s}_{d,co}$ can be written as

$$\mathbf{s}_{d,co} = n_a/n_d\ \mathbf{s}_i + (n_a/n_d\ \cos\theta_{ad} - \cos\psi_{ad})\ \mathbf{n}_{d,c}, \qquad (20)$$

where θ_{ad} and ψ_{ad} are the angles of incidence and refraction at the air/droplet interface, given by $\cos\theta_{ad} = |\mathbf{s}_i \cdot \mathbf{n}_{d,c}|$ and $n_a \sin\theta_{ad} = n_d \sin\psi_{ad}$. Finally, the unit vector of the transmitted ray $\mathbf{s}_{t,co}$ through the window, which corresponds to the cutoff angle, can be expressed as

$$\begin{aligned}\mathbf{s}_{t,co} &= n_d/n_a\ \mathbf{s}_{d,co} + (n_d/n_a\ \cos\theta_{dw} - \cos\psi_{wa})\ \mathbf{n}_w \\ &= \left[\cos\varphi^E_{t,co}\sin\theta^E_{t,co},\ \sin\varphi^E_{t,co}\sin\theta^E_{t,co},\ \ -\cos\theta^E_{t,co}\right]^{\mathrm{T}},\end{aligned} \qquad (21)$$

where $\mathbf{n}_w = [0,\ 0,\ 1]^{\mathrm{T}}$ is the unit vector of the upper normal on the window's surface, θ_{dw} is the angle of incidence at the droplet/window interface, and ψ_{wa} the angle of refraction at the window/air interface, defined respectively by $\cos\theta_{dw} = |\mathbf{s}_{d,co} \cdot \mathbf{n}_w|$ and $n_d \sin\theta_{dw} = n_a \sin\psi_{wa}$. For every azimuthal angle $\varphi_{n,c}$ of the unit vector of the outer normal $\mathbf{n}_{d,c}$, a pair of cutoff polar and azimuthal angles $(\theta^E_{t,co}, \varphi^E_{t,co})$ can be predicted implicitly from Eq. (21). In fact, Fig. 11(c) establishes that the predictions of Eq.(21) were in excellent agreement with numerical simulations obtained from Monte Carlo ray tracing method.

Similarly, Fig. 12(b) shows a window with droplets on its backside exposed to collimated radiation with incident direction $\mathbf{s}_i$ given by Eq. (18). Then, the unit direction vector of the ray transmitted inside the droplet $\mathbf{s}_{d,c}$ through the window incident on the contact line of the droplet can be expressed as

$$\mathbf{s}_{d,c} = n_a/n_d\ \mathbf{s}_i + (n_a/n_d\ \cos\theta_{aw} - \cos\psi_{wd})\ \mathbf{n}_w, \qquad (22)$$

where θ_{aw} is the angle of incidence at the air/window interface and ψ_{wd} the angle of refraction at the window/droplet interface, given by $\cos\theta_{aw} = |\mathbf{s}_i \cdot \mathbf{n}_w|$ and $n_a \sin\theta_{aw} = n_d \sin\psi_{wd}$. Here also, $\theta_{n,c} = \theta_c$ and $\varphi_{n,c} \in [\varphi_i - \pi/2,\ \varphi_i + 3\pi/2]$, while $\varphi_{n,c} \in [\varphi_i - \pi/2,\ \varphi_i + \pi/2]$ corresponds to the large cutoff angle $\theta^{B,+}_{t,co}$ and $\varphi_{n,c} \in [\varphi_i + \pi/2,\ \varphi_i + 3\pi/2]$ to the small cutoff angle $\theta^{B,-}_{t,co}$, as illustrated in Fig. 8. Then, the unit vector $s_{t,co}$ of the transmission ray corresponding to the cutoff angles $\theta^B_{t,co}$ and $\varphi^B_{t,co}$ are given by

$$\begin{aligned}\mathbf{s}_{t,co} &= \mathbf{s}_{d,co} n_d/n_a + (\cos\theta_{da} n_d/n_a - \cos\psi_{da})\ \mathbf{n}_{d,c} \\ &= \left[\cos\varphi^B_{t,co}\sin\theta^B_{t,co},\ \sin\varphi^B_{t,co}\sin\theta^B_{t,co},\ \ -\cos\theta^B_{t,co}\right]^{\mathrm{T}},\end{aligned} \qquad (23)$$

where θ_{da} and ψ_{da} are the angles of incidence and refraction at droplet/air interface, given by $\cos\theta_{da} = |\mathbf{s}_{d,c} \cdot \mathbf{n}_{d,c}|$ and $n_d \sin\theta_{da} = n_a \sin\psi_{da}$. Here, the unit vector of the inner normal on the contact line of the droplet $\mathbf{n}_{d,c}$ is given by Eq. (18). Finally, we can obtain an implicit relationship between the cutoff polar angle $\theta^B_{t,co}$ and the cutoff azimuthal angle $\varphi^B_{t,co}$ using Eq. (23), as shown in Fig. 11(d). Here also, excellent agreement was observed between

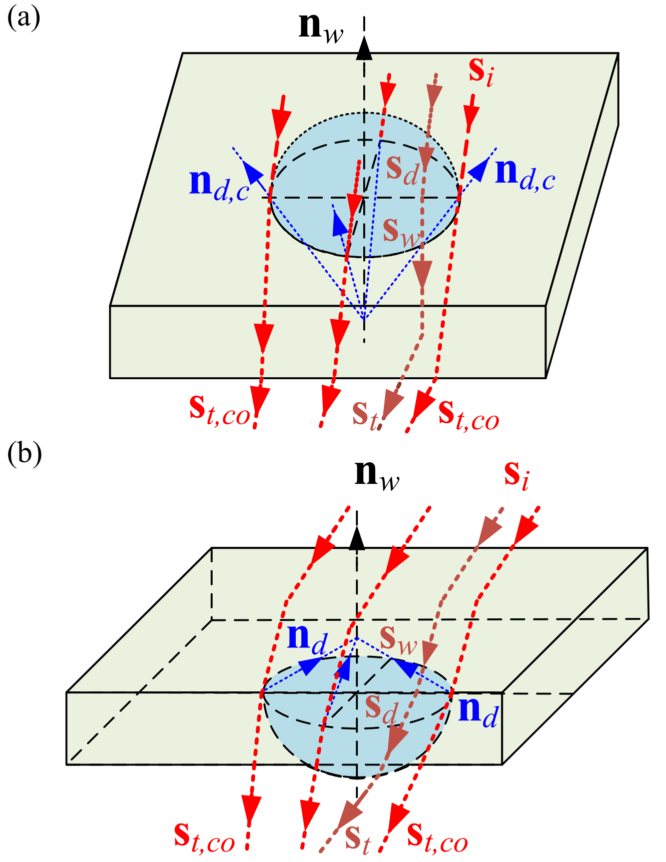

Fig. 12. Schematic illustrating the three-dimensional ray propagation through the window with (a) external droplets and (b) backside droplets for the relationship between the cutoff polar angle and cutoff azimuthal angle.

numerical simulations and analytical predictions of Eq. (23), as illustrated in Fig. 11(d).

5. Conclusion

This study numerically investigated the bidirectional transmittance of transparent windows covered with nonabsorbing cap-shaped droplets either on their front side or on their back side. The effects of the droplet spatial and size distributions, contact angle and of the incident polar and azimuthal angles on the bidirectional transmittance were assessed systematically. First, the one-dimensional bidirectional transmittance for droplets on either front or back side was found to be independent of droplet spatial and size distributions. In addition, in both cases, the one-dimensional bidirectional transmittance had a sharp peak in the transmission direction equals to the incident direction. This peak corresponded to the photons incident on the dry part of the window and did not interact with the droplets. Moreover, the one-dimensional bidirectional transmittance of windows with droplets on its front or back featured large and/or small cutoff transmission angles beyond which the transmission decreased sharply. Analytical predictions of the cutoff angles in the different configurations were derived along with the conditions for their existence on the incident angle and droplet contact angle. In addition, the one-dimensional bidirectional transmittance increased with increasing projected surface area coverage at other transmission angles while it decreased in the incident directions. Finally, the bidirectional transmittance was axisymmetric with respect to the plane of incidence so that the rays were scattered into other transmission azimuthal angle around the incident azimuthal angle. These results will be useful in the discovery and selection of materials and surface coatings to improve light transmission of optical windows, solar energy conversion systems, as well as the image quality of camera lenses.

Declaration of Competing Interest

We declare that we do not have any commercial or associative interest that represents a conflict of interest in connection with the work submitted.

CRediT authorship contribution statement

Yong Huang: Methodology, Supervision, Funding acquisition. **Chenxi Feng:** Data curation, Writing - original draft. **Jack Hoeniges:** Data curation. **Keyong Zhu:** Conceptualization, Writing - review & editing, Formal analysis, Funding acquisition. **Laurent Pilon:** Conceptualization, Writing - review & editing, Funding acquisition.

Acknowledgements

This study was supported in part by the National Natural Science Foundation of China (Nos. 51406006 and 51876004), the Fundamental Research Funds for Central Universities (No. YWF-20-BJ-J-818), and the U.S. Advanced Research Project Agency–Energy (DE-AR0000738).

Supplementary materials

Supplementary material associated with this article can be found, in the online version, at doi:10.1016/j.jqsrt.2020.107039.

References

[1] Zhang L, Li Y, Sun J, Shen J. Mechanically stable antireflection and antifogging coatings fabricated by the layer-by-layer deposition process and postcalcination. Langmuir 2008;24:10851–7.
[2] Li Y, Zhang J, Zhu S, Dong H, Jia F, Wang Z, et al. Biomimetic surfaces for high-performance optics. Adv Mater 2009;21:4731–4.
[3] Chevallier P, Turgeon S, Sarra-Bournet C, Turcotte R, Laroche G. Characterization of multilayer anti-fog coatings. ACS Appl Mater Interfaces 2011;3:750–8.
[4] Zhao J, Ma L, Millians W, Wu T, Ming W. Dual-functional antifogging/antimicrobial polymer coating. ACS Appl Mater Interfaces 2016;8:8737–42.
[5] Han Z, Feng X, Guo Z, Niu S, Ren L. Flourishing bioinspired antifogging materials with superwettability: progresses and challenges. Adv Mater 2018;30:e1704652.
[6] Geoola F, Kashti Y, Peiper UM. A model greenhouse for testing the role of condensation, dust and dirt on the solar radiation transmissivity of greenhouse cladding materials. J Agric Eng Res 1998;71:339–46.
[7] Chaibi MT, Jilar T. Effects of a solar desalination module integrated in a greenhouse roof on light transmission and crop growth. Biosystems Eng 2005;90:319–30.
[8] Zhang X-T, Sato O, Taguchi M, Einaga Y, Murakami T, Fujishima A. Self-cleaning particle coating with antireflection properties. Chem Mater 2005;17:696–700.
[9] Cemek B, Demir Y. Testing of the condensation characteristics and light transmissions of different plastic film covering materials. Polym Test 2005;24:284–9.
[10] Hautière N, Dumont E, Brémond R, Ledoux V. Review of the mechanisms of visibility reduction by rain and wet road. In: International Symposium on Automotive Lighting; 2009. p. 445–55.
[11] Nair G, Mahapatra K, Gustavsson L. Implementation of energy-efficient windows in Swedish single-family houses. Appl Energy 2012;89:329–38.
[12] Zhang X, He J. Antifogging antireflective thin films: does the antifogging layer have to be the outmost layer? Chem Commun 2015;51:12661–4.
[13] Nomura K, Oshima H, Yamauchi D, Hidaka H, Kawase T, Katori Y. Ototoxic effect of ultrastop antifog solution applied to the guinea pig middle ear. Otolaryngol Head Neck Surg 2014;151:840–4.
[14] Wang S, Liu K, Yao X, Jiang L. Bioinspired surfaces with superwettability: new insight on theory, design, and applications. Chem Rev 2015;115:8230–93.
[15] Xu L, He J. Antifogging and antireflection coatings fabricated by integrating solid and mesoporous silica nanoparticles without any post-treatments. ACS Appl Mater Interfaces 2012;4:3293–9.
[16] Li Y, Fang X, Wang Y, Ma B, Sun J. Highly transparent and water-enabled healable antifogging and frost-resisting films based on poly (vinyl alcohol)–nafion complexes. Chem Mater 2016;28:6975–84.

[17] Heinemann PH, Walker PN. Effects of greenhouse surface heating water on light transmission. Trans ASAE 1987;30:215–20.

[18] Jaffrin A, Morisot A. Mechanism of light transmission through wet polymer films. Acta Hortic. 1990;281:11–24.

[19] Cebeci FC, Wu Z, Zhai L, Cohen RE, Rubner MF. Nanoporosity-driven superhydrophilicity: a means to create multifunctional antifogging coatings. Langmuir 2006;22:2856–62.

[20] Wen M, Wang L, Zhang M, Jiang L, Zheng Y. Antifogging and icing-delay properties of composite micro- and nanostructured surfaces. ACS Appl Mater Interfaces 2014;6:3963–8.

[21] Di Mundo R, d'Agostino R, Palumbo F. Long-lasting antifog plasma modification of transparent plastics. ACS Appl Mater Interfaces 2014;6:17059–66.

[22] Crebolder JM, Sloan RB. Determining the effects of eyewear fogging on visual task performance. Appl Ergon 2004;35:371–81.

[23] Howarter JA, Youngblood JP. Self-cleaning and next generation anti-fog surfaces and coatings. Macromol Rapid Commun 2008;29:455–66.

[24] Lee H, Alcaraz ML, Rubner MF, Cohen RE. Zwitter-wettability and antifogging coatings with frost-resisting capabilities. ACS Nano 2013;7:2172–85.

[25] Zhu K, Li S, Pilon L. Light transfer through windows with external condensation. J Quant Spectrosc Radiat Transfer 2018;208:164–71.

[26] Zhu K, Huang Y, Pruvost J, Legrand J, Pilon L. Transmittance of transparent windows with non-absorbing cap-shaped droplets condensed on their backside. J Quant Spectrosc Radiat Transfer 2017;194:98–107.

[27] Briscoe BJ, Galvin KP. The effect of surface fog on the transmittance of light. Sol Energy 1991;46:191–7.

[28] Werner A, Roos A. Condensation tests on glass samples for energy efficient windows. Sol Energy Mater Sol Cells 2007;91:609–15.

[29] Zhu K, Pilon L. Transmittance of semitransparent windows with absorbing cap-shaped droplets condensed on their backside. J Quant Spectrosc Radiat Transfer 2017;201:53–63.

[30] Pollet IV, Pieters JG. Forward scattering induced by water drops on a transmissive substrate. Appl Opt 2002;41:5122–9.

[31] Pollet IV, Pieters JG, Deltour J, Verschoore R. Diffusion of radiation transmitted through dry and condensate covered transmitting materials. Sol Energy Mater Sol Cells 2005;86:177–96.

[32] Bhardwaj R, ten Kortenaar MV, Mudde RF. Influence of condensation surface on solar distillation. Desalination 2013;326:37–45.

[33] Khalifa AJN. On the effect of cover tilt angle of the simple solar still on its productivity in different seasons and latitudes. Energy Convers Manage 2011;52:431–6.

[34] Rubio E, Fernández-Zayas JL, Porta-Gándara MA. Current status of theoretical and practical research of seawater single-effect passive solar distillation in mexico. J Mar Sci Eng 2020;8:94.

[35] Pruvost J, Cornet JF, Goetz V, Legrand J. Theoretical investigation of biomass productivities achievable in solar rectangular photobioreactors for the cyanobacterium Arthrospira platensis. Biotechnol Prog 2012;28:699–714.

[36] Soulies A, Legrand J, Marec H, Pruvost J, Castelain C, Burghelea T, et al. Investigation and modeling of the effects of light spectrum and incident angle on the growth of Chlorella vulgaris in photobioreactors. Biotechnol Prog 2016;32:247–61.

[37] Eigen D, Krishnan D, Fergus R. Restoring an image taken through a window covered with dirt or rain. In: 2013 IEEE International Conference on Computer Vision; 2013. p. 633–40. ..

[38] Edwards RI, Lake JV. The transmission of solar radiation in a small east-west glasshouse glazed with diffusing glass. J Agric Eng Res 1965;10:197–201.

[39] De Gennes P.G., Brochard-Wyart F., Quéré D. Capillarity and wetting phenomena: drops, bubbles, pearls, waves: springer science & business media; 2013.

[40] Khandekar S, Muralidhar K. Dropwise condensation on inclined textured surfaces. Spinger; 2014.

[41] Howell JR, Mengüç MP, Siegel R. Thermal radiation heat transfer. 6th ed. Taylor and Francis: CRC Press; 2016.

[42] Modest MF. Radiative heat transfer. 3rd ed. New York: Academic Press; 2013.